WELDING RESEARCH

SUPPLEMENT TO THE *WELDING JOURNAL*, OCTOBER 1997
Sponsored by the American Welding Society and the Welding Research Council

Stainless Steel Cladding Deposited by Automatic Gas Metal Arc Welding

Color metallography, along with ferrite measurement, EPMA, and SEM analysis, revealed explicitly the different solidification phases in stainless steel cladding

BY N. MURUGAN AND R. S. PARMAR

ABSTRACT. Weld surfacing is increasingly employed to enhance the life of and to reduce the cost of engineering components. Gas metal arc (GMA) cladding is extensively applied in its automatic mode to obtain good quality stainless steel claddings. In stainless steel cladding, the amount of dilution and the mode of solidification of claddings are vital factors affecting the quality of claddings. Developed mathematical models relating GMAW process control parameters to cladding dimensions were used to deposit 316L and 309L stainless steel on structural steel IS:2062 and obtained 12% dilution in single layer claddings. The metallurgical features, such as cladding chemistry, microstructures, modes of solidifications, ferrite content, transition zone chemistry, etc., of single and multilayer claddings were analyzed.

Controlled dilution level (12%) facilitated the achievement of the required levels of alloy content meeting corrosion resistance requirements and producing crack-free claddings. The hardness of the transition zone was found to be below 400 VHN due to low-carbon levels used in stainless steel filler metals and lower dilution achieved in cladding. Cladding solidified initially with planar or cellular structure and then gradually changed to cellular-dentritic structure depending upon the heat input condition and the dilution involved. Color metallography revealed three modes of solidification of stainless steel claddings and observed modes of solidification were in good agreement with the predicted modes. Estimated ferrite contents were also in close agreement with their corresponding measured values. Two types of ferrite morphology such as vermicular and lathy were found, and, at higher ferrite content levels, lathy morphology was predominant.

N. MURUGAN is a Senior Lecturer, Dept. of Mech. Eng., Coimbatore Institute of Technology, Coimbatore, India, and R. S. PARMAR is a Professor of Mech. Eng., I.I.T., New Delhi, India.

KEY WORDS

Weld Surfacing
Stainless Steel Cladding
Microstructure
Microhardness
Modes of Solidification
Delta Ferrite
EPMA
Color Etching

Introduction

Weld surfacing is popularly employed to increase corrosion resistance, wear resistance, resistance to high temperature, etc., at the surface of a component in order to enhance its life and to reduce its cost by depositing a suitable filler material. It is not only applied in the maintenance and repair industry but also increasingly exploited in the fabrication of components in power and process industries. Weld surfacing techniques can be classified according to properties conferred by the surface coating. They are called cladding, hardfacing, buildup, and buttering to achieve corrosion resistance (for chemical wear), wear resistance (for physical wear), dimensional control (to rebuild worn components), and metallurgical needs, respectively. Among the materials employed for surfacing, stainless steel is perhaps the most popular for corrosion and heat resisting service due to its remarkable ductility, strength, toughness and ease of welding.

The internal surfaces of paper digesters, urea reactors, atomic reactor containment vessels and pressurizers, and hydrocrackers, to name some of the more spectacular examples, are often clad by welding to produce a corrosion resistant surface (Ref. 1).

Among the various processes employed for surfacing, such as shielded metal arc welding (SMAW), submerged arc welding (SAW), gas metal arc welding (GMAW), gas tungsten arc welding (GTAW), plasma arc welding (PAW), electroslag welding (ESW), etc., the

GMAW process has become the cost-effective choice for surfacing smaller and medium sized areas due to its superior quality, ease of use, ease of mechanization and all-position capability.

The most important aspect in any fusion cladding application is the dilution of the filler metal by the base metal resulting in the reduction of the filler material's properties. The control of dilution plays a vital role in the economics of the weld cladding process due to the high cost of the highly alloyed filler metal. Also, there should be a minimum amount of dilution required to satisfy the bond strength between the cladding and the base metal. The recommended minimum dilution is 10 to 15% (Ref. 2). In the case of stainless steel cladding, the ferrite content of the cladding should also meet the recommended values, depending on the type of stainless steel, to avoid microfissuring. The amount of ferrite that is present will essentially depend upon the chemical composition of the filler and the base metals, type of welding process and the probable variation of the process parameters during welding or cladding. The ferrite content that can be allowed in a weld is usually decided by considering its effects like hot cracking, sigma phase embrittlement and corrosion behavior.

Over a period of years, recognition of the potency of ferrite content in eliminating weld cracking has resulted in the development of empirical diagrams such as Schaeffler and DeLong for predicting weld ferrite content from alloy composition. A new WRC-1992 constitutional diagram has also been developed to predict the microstructure, ferrite content and mode of solidification of stainless steels from its chemical equivalents (Ref. 3). This also helps to select proper filler materials to weld different stainless steels as well as in dissimilar welding and cladding.

It has been generally accepted that welds, like casting, can solidify with primary phase being either ferrite or austenite. It is also becoming generally accepted that primary ferrite solidified welds are more crack resistant than primary austenite solidified welds, solidification mode is the most important factor in deciding the cracking tendency, as weld solidification cracking in a stainless steel is related to not only the amount of ferrite present at room temperature but also its solidification mode (Ref. 4). Hence, it is essential to have not only lower dilution in the claddings but also to know the primary solidification modes that could occur in the claddings. The modes of solidification that occur in stainless steels are illustrated in Fig. 1 (Ref. 2).

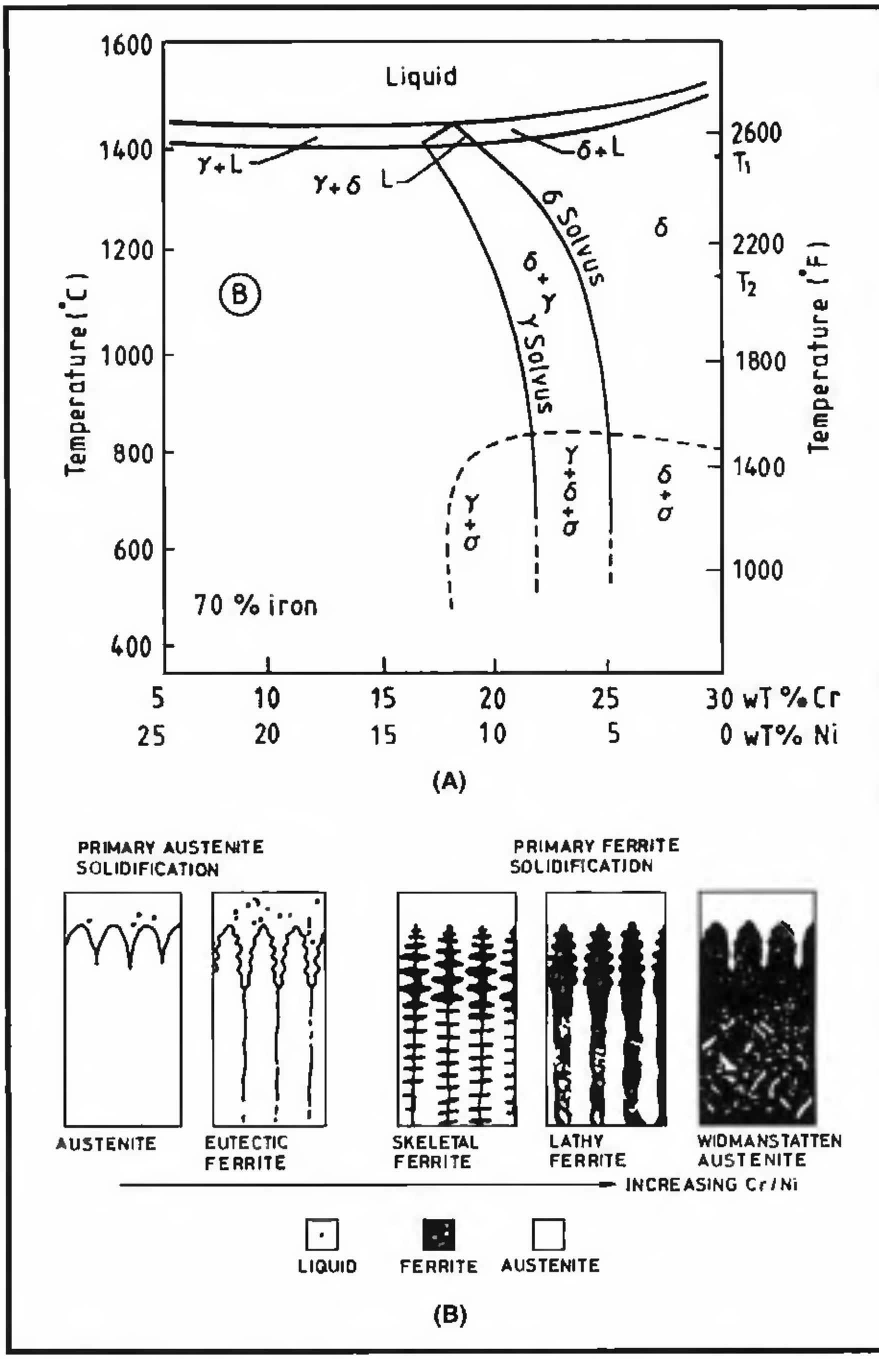

Fig. 1—A—70% iron vertical section of Fe-Cr-Ni ternary diagram; B—Modes of solidification of austenitic stainless steels (Ref. 2).

Lower dilution may be obtained by the proper selection of process parameters using developed mathematical expressions/models relating the weld bead dimensions to the important controllable process parameters affecting the bead dimensions. The development of such models will further facilitate in optimizing the process parameters to have low dilution and crack-free cladding.

In practice, the ill effects of high dilution of single stainless steel claddings have been overcome by the use of multiple claddings, or by using consumables more highly alloyed in chromium and nickel, generally 309 or 309L, for the first pass in direct contact with the substrate material. However, a thorough understanding of the process characteristics affecting the technological and metallurgical characteristics of the cladding will assist in achieving better quality claddings. Hence, to establish a better cladding procedure, mathematical models had been developed and the direct and interaction effects of various GMAW process parameters affecting cladding dimensions were analyzed.

Table 1—Chemical Composition of Base and Filler Materials

Sl. No.	Description	Material	Chemical composition (Wt-%) C	Mn	Si	Cr	Ni	Mo	Cu	S	P
1	Base Metal	IS:2062	0.250	1.60	—	—	—	—	—	0.055	0.055
2	Filler Metal Batch I	316L	0.016	1.55	0.36	18.55	12.15	2.15	0.016	0.006	0.012
3	Filler Metal Batch II	316L	0.018	1.59	0.35	18.15	12.78	2.2	0.100	0.008	0.025
4	Filler Metal	309L	0.019	1.76	0.41	23.49	13.32	0.75	—	0.004	0.023

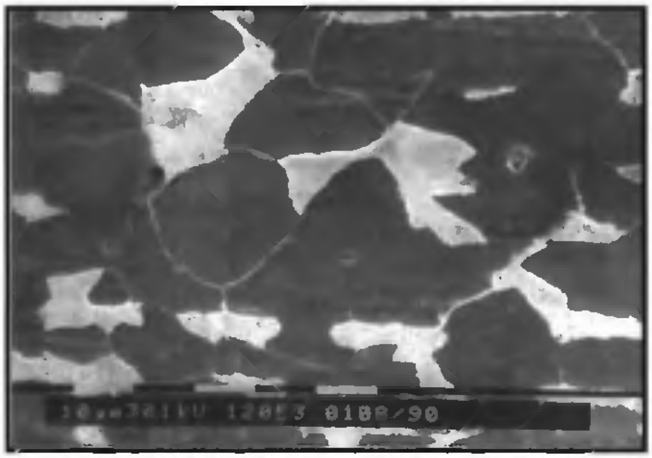

Fig. 2—Microstructure of structural steel base metal showing pearlite colonies in a ferrite matrix (X1200).

Fig. 3—Transverse section of a typical multipass single layer cladding.

These are well detailed in Refs. 5–7.

From the developed models, necessary GMAW process control parameters were chosen to achieve lower dilution in 316L stainless steel single as well as multipass cladding. The success of the cladding procedure employed was analyzed by carrying out the metallurgical analysis, mechanical testing and corrosion testing of claddings. This paper highlights the metallurgical analysis of claddings deposited at lower dilution conditions. The mechanical and corrosion testing of claddings were presented in detail in Refs. 7 and 8.

Experimental Procedure

Materials Used

Structural steel IS:2062 was used as the base material whose composition is given in Table 1 and its microstructure is shown in Fig. 2. The base plate of 20 mm thickness was cut into 250 mm x 150 mm size and the surfaces were ground to remove oxide scale and dirt. The claddings were deposited by using 1.2 mm dia. 316L and 309L stainless steel wire electrodes with industrially pure Argon as shielding gas.

Surfacing

A computer controlled automatic MIG surfacing system (Ref. 9) was employed to surface the structural steel plate with stainless steels by depositing four beads with about 30% overlap. The welding parameters used were predicted from mathematical models developed (Ref. 7) to obtain lower dilution in the claddings. The interpass temperature was maintained at about 100°C. Multilayer surfacing was also carried out using the same process parameters. Sample codes were used to identify the specimens prepared from the different claddings deposited. A typical cross section of a multipass single layer cladding is shown in Fig. 3.

Analysis of Chemistry of Claddings

The chemical composition of the samples mentioned above were analyzed using a Spectrovac system based on the atomic emission analytical technique. The top surfaces of the samples were ground flat for 2 mm depth and three test burns were taken to find out the chemical composition of the important elements present in the cladding. The average of the three readings were calculated and tabulated for various elements as shown in Table 2.

Microhardness Survey

Standard metallurgical procedures were used to prepare the samples for microhardness studies and were etched suitably to facilitate microhardness surveys along the different metallurgical zones of the cladding such as unaffected base metal, HAZ, transition zone and clad metal. A Wolpert Microhardness Tester was employed to carry out microhardness survey on various parts of the as-welded specimens which were cut perpendicular to welding direction, starting from the base metal up to the weld metal farthest from the fusion line along the centerline of a single bead as well as across two adjacent beads. A Vickers indenter with 100 g load was used to make indentations on all specimens. The microhardness values obtained were plotted against the distance covered along its different zones in graphical form for quick analysis; a few of these hardness traverses are shown in Figs. 4–10.

Ferrite Measurement

The top surfaces of all specimens obtained from the cladded plates were ground flat and the delta ferrite contents of the clads in the as-welded condition were measured using a Ferritescope. Six readings were taken on the top of specimens in transverse and longitudinal directions and the average values of ferrite content are given in Table 3.

Metallography

Standard metallurgical procedures were employed to prepare all samples and color metallography was used to reveal various phases present in all zones of the claddings. Since color etching makes both primary and secondary structures visible (Refs. 10, 11), it was especially employed for stainless steel weld metal to assess the modes of solidification. The etchants and the etching conditions for mild steel base metal as well as stainless steel weld metal are given in Table 4 (Refs. 12,13). The color etchant 2 (a) was used almost in all cases as it gave better reproducibility of results.

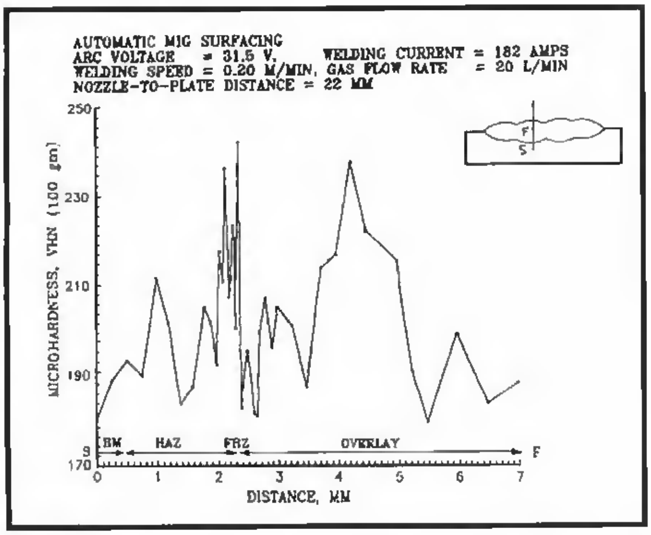

Fig. 4—Microhardness traverse in single layer 316L SS cladding (J1). Insert shows path of hardness traverse.

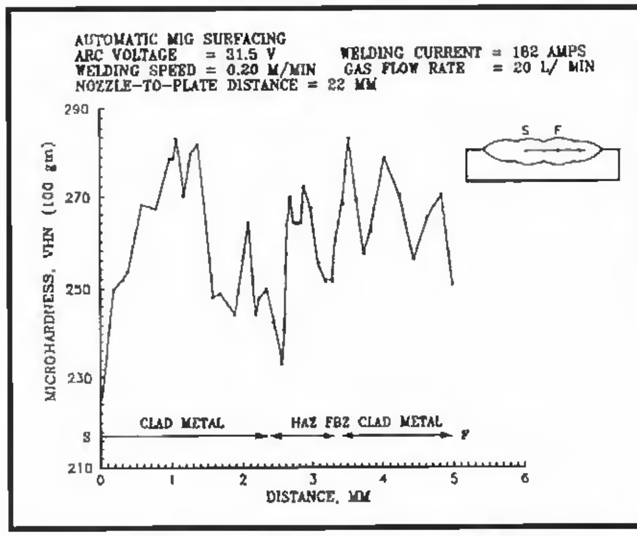

Fig. 5—Microhardness traverse in single layer 316L SS cladding (J1). Insert shows path of hardness traverse.

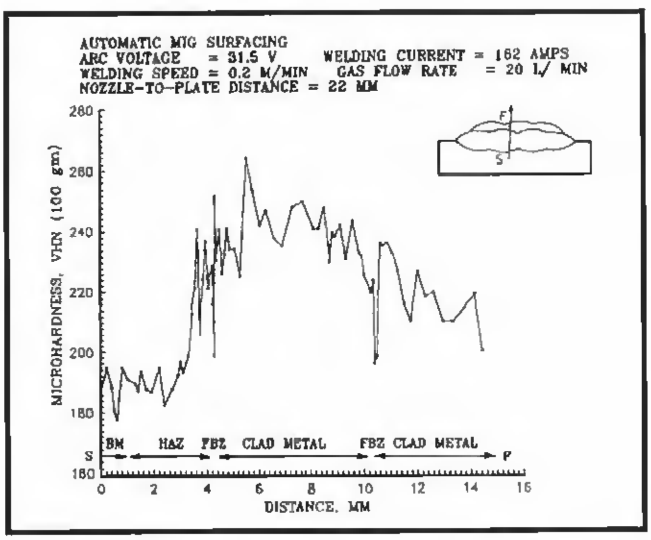

Fig. 6—Microhardness traverse in double layer 316L SS cladding (J2). Insert shows path of hardness traverse.

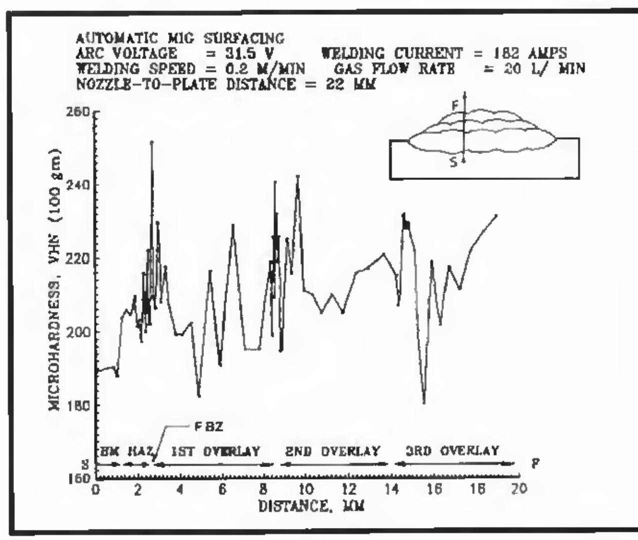

Fig. 7—Microhardness traverse in multilayer 316L SS cladding (J3). Insert shows path of hardness traverse.

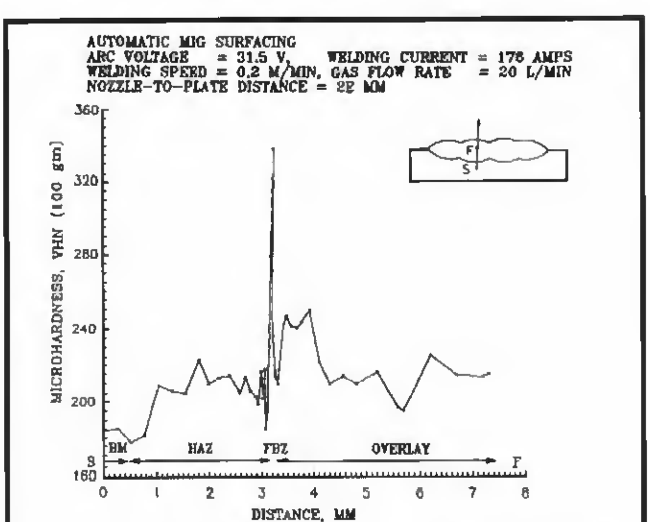

Fig. 8—Microhardness traverse in single layer 309L SS cladding (J4). Insert shows path of hardness traverse.

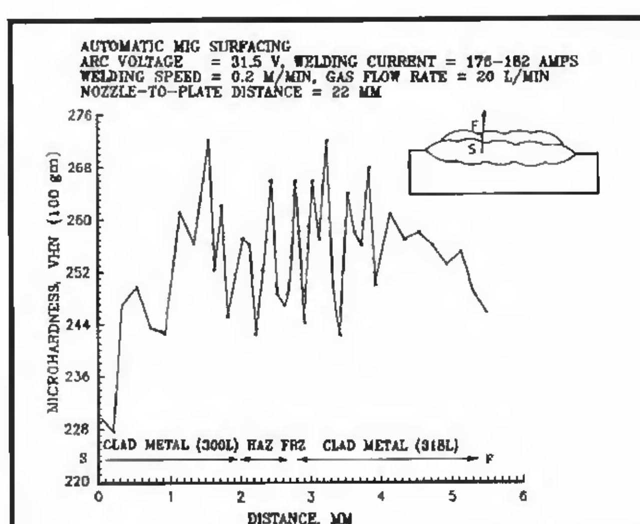

Fig. 9—Microhardness traverse in double layer 316L SS cladding (J7). Insert shows path of hardness traverse.

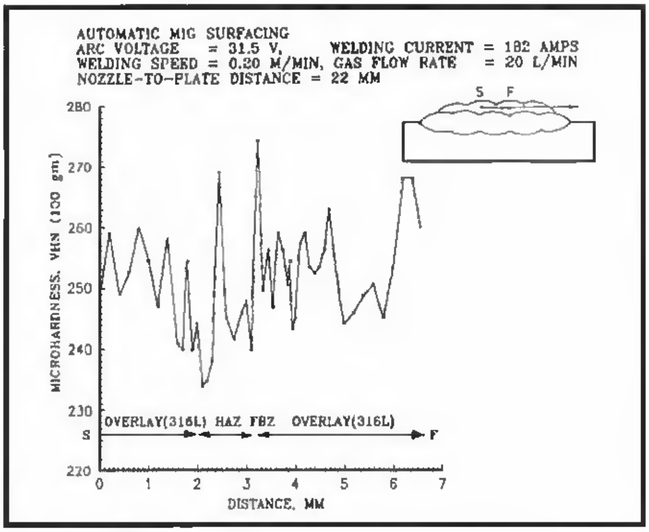

Fig. 10—Microhardness traverse in multilayer 316L SS cladding (J7). Insert shows path of hardness traverse.

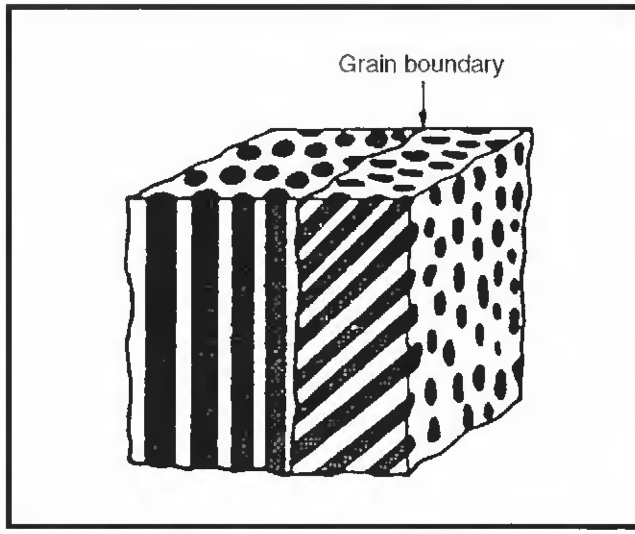

Fig. 11—Effect of sectioning on solidification structure (Ref. 20).

Table 2—Chemical Compositinn of Stainless Steel Overlays

Sample Code	Material	C	Si	Mn	Cr	Ni	Mo	Cu	Nb	Ti	Remarks
		Elements, Wt-%									
J1	316L	0.027	0.303	1.591	16.419	12.154	2.116	0.104	0.004	0.002	One Layer Batch II
J2	316L	0.021	0.333	1.674	17.983	12.858	2.235	0.128	0.013	0.015	Two Layer Batch II
J3	316L	0.019	0.333	1.704	18.338	12.727	2.300	0.122	0.013	0.015	Three Layers Batch II
J4	309L	0.023	0.489	1.674	21.153	11.548	0.091	0.095	0.001	0.004	One Layer
J7	316L	0.022	0.320	1.610	17.980	12.640	2.012	0.104	—	—	FL 309 and SL 316L Batch II
J8	316L	0.018	0.374	1.595	17.780	11.860	1.850	0.020	—	—	FL 309L and SL 316L Batch I

FL = First Layer
SL = Second Layer

Table 3—Comparison of Predicted and Measured Ferrite Content of Stainless Steel Claddings

Sl. No.	Sample Code	SDF, %	DDF, %	DDF, FN	WDF, FN	SEF, %	%	FN
		Predicted Ferrite Content					Measured Ferrite Content	
1	J1	0.0	0.0	0.0	0.0	−1.6	2.92	2.92
2	J2	2.0	0.5	0.5	1.8	2.4	5.92	5.92
3	J3	3.9	1.7	1.7	2.5	3.9	6.35	6.42
4	J4	8.5	7.0	7.2	6.7	9.4	6.65	6.78
5	J7	1.0	0.0	0.0	1.3	2.1	6.65	6.78
6	J8	4.3	0.5	0.5	1.9	3.7	1.13	1.13

SDF = Predicted ferrite content based on Schaeffler Diagram
DDF = Predicted ferrite content based on Delong Diagram
WDF = Predicted ferrite content based on WRC-1992 Diagram
SEF = Predicted ferrite content based on Seferian Equation
= $3\,(Cr_{equ.} - 0.93\,Ni_{equ.} - 6.7)$, where $Cr_{equ.}$ and $Ni_{equ.}$ are defined as in Schaeffler Diagram

The etched samples were subjected to an extensive microstructure survey using a Vickers M-17 optical microscope to study the microstructure in base metal, HAZ, fusion line and clad metal under different magnifications ranging from 100X to 1000X. Many zones of interest were photographed to study the extent of coalescence as well as the type and nature of microstructure present. However, to keep the length of the paper within limit only a selected few are presented (Figs. 12–21).

EPMA and SEM Analysis

To investigate the constitution of the fusion boundary between the plate and the first layer of cladding and also along dendrites of δ-iron precisely, an electron probe microanalyzer, Joel JXA-8600 was used. The specimens prepared for microstructural studies were used for EPMA and SEM studies and they were etched with the etchant 2(a) given in Table 4. The X-ray intensities of Cr, Ni, Mn, Mo, P, S, and Fe were obtained by line method along fusion zones of cladded samples and along dendrites of δ-iron present in the microstructure of the samples. The

Table 4—Etchants for Base Metal and Weld Cladding

Sl. No.	Description	Material	Etchant
1	Base Metal	IS:2062	A—2% Nital B—50 mL cold-saturated sodium thiosulphate solution and 1 g potassium metabisulfite
2	Weld Overlays	316L 309L	A—20 g ammonium biflouride and 0.5 g potassium metabisulfite in 100 mL distilled water at 40°C B—Stock solution: 1:5 v/v hydrochloric acid (35%) and distilled water. 100 mL of the stock solution plus 0.5–1 g potassium metabisulfite.

Table 5—Chromium and Nickel Equivalents of Claddings

		Chemical Equivalents, %							
Sl. No.	Sample Code	SCE	SNE	DCE	DNE	HCE	HNE	WCE	WNE
1	J1	19.0	13.8	19.0	16.2	19.8	16.1	18.5	14.7
2	J2	20.8	14.3	20.8	16.7	21.8	16.8	20.3	15.2
3	J3	21.1	14.1	21.1	16.5	22.1	16.6	20.6	15.0
4	J4	22.0	13.1	22.0	15.5	22.0	15.5	21.2	14.0
5	J7	20.5	14.1	20.5	16.5	21.2	16.5	20.0	15.0
6	J8	20.2	13.2	20.2	15.6	20.9	15.5	19.6	14.1

SCE, Schaeffler Chromium Equivalent = % Cr + % Mo + 1.5% Si + 0.5% Nb
SNE, Schaeffler Nickel Equivalent = % Ni + 30% C + 0.5% Mn
DCE, Delong Chromium Equivalent = % Cr + % Mo + 1.5% Si + 0.5% Nb
DNE, Delong Nickel Equivalent = % Ni + 30% C + 30% N + 0.5% Mn
HCE, Hammer and Svensson Chromium Equivalent = % Cr + 1.37% Mo + 1.5% Si + 2% Nb + 3% Ti
HNE, Hammer and Svensson Nickel Equivalent = % Ni + 22% C + 14.2% N + 1.31% Mn + % Cu
WCE, WRC-1992 Diagram Chromium Equivalent = % Cr + % Mo + 0.7% Nb
WNE, WRC-1992 Diagram Nickel Equivalent = % Ni + 35% C + 20% N + 0.25% Cu

photomicrographs of the various zones as well as dendrites of delta iron selected for analysis were obtained at different magnifications using the SEM which was attached to the analyzer; a few of them are presented to identify the location of the line analysis carried out.

Results and Discussions

Analysis of Chemistry of Claddings

From Table 2, the potential factors or equivalents of Schaeffler, Delong, WRC 1992 Constitutional Diagrams were calculated and tabulated as shown in Table 5. As analysis of nitrogen was not possible, it was taken as 0.08% for MIG process (Refs. 2, 14). It is evident from Table 2 that chemical composition of the cladding depends on the amount of dilution caused by the intermixing of base metal and the filler metal. For example, alloy content of clad metal increased from the first layer to second layer (Samples J1, J2). The composition of second and third cladding meets the required specification of ER316L stainless steel to satisfy the required corrosion resistance of the cladding. The carbon content of claddings was all well within the maximum limit of 0.03 wt-%, attributable to the fact that the dilutions achieved in single layer surfacing were 12.43% and 11.79% respectively in 316L (J1) and 309L (J4) claddings.

Analysis of Microhardness Survey

The microhardness survey carried out in various zones of multipass stainless steel claddings along the centerline of single beads and across two adjacent beads for double bead claddings is presented in the form of graphs in Figs. 4–10. In all these figures, the hardness curve has been divided into four parts: 1) unaffected base metal (BM), 2) heat affected zone (HAZ), 3) fusion boundary zone (FBZ), and 4) cladding or weld metal (WM).

It is evident from the figures that the microhardness values of HAZ, particularly the coarse grained region of HAZ, were higher than the unaffected base metal. This may be due to the formation of bainitic structure in HAZ. In all cases, the hardness of HAZ close to the fusion boundary zone was found to be less than the peak hardness values of HAZ. This could possibly be due to the formation of coarse bainite.

In the FBZ, the hardness suddenly increased to a high value and then dropped abruptly to a lower value. This increase in hardness was due to the presence of martensite. The dilution was relatively more in those zones and the corresponding composition gradients of the transition zone normally cut across the composition range of martensite in Schaeffler Diagram (Refs. 2, 13). Because of composition gradient, the transition zone between austenitic cladding and base metal (carbon steel) was martensitic, its hardness dependent upon the carbon content of the zone. In the as-welded condition the carbon content in this martensitic zone was relatively low and the hardness was, therefore, low; and the case was the same for most of the claddings. The peak hardness of FBZ of claddings surfaced by using 316L stainless steel wire was found to be below 300 VHN, possibly attributable to the utilization of low dilution procedure and low carbon grade filler wire.

On entering the cladding region, the hardness decreased drastically from the peak value and then varied depending upon the conditions of welding. The hardness of claddings was well below 300 VHN which indicates better toughness and ductility of clad metal.

From Figs. 5 and 10, it is apparent that the hardness values of the weld metal as well as the reheated and remelted portions of weld metal, due to multipass surfacing, were not appreciably altered. This could possibly be due to lower welding speed employed for surfacing resulting in lower cooling rate. Also, Figs. 6, 7, and 9 represent not only multipass condition but also multilayer condition, and in those claddings there is no significant change in hardness of cladding. This may signal the absence of carbides and σ-phase formation. Carbides were not expected because of the low carbon content of the weld deposit, as seen from Table 2, owing to the use of low carbon grade filler materials (<0.02%-wt C). In austenitic stainless steel multirun claddings there were areas exposed, during thermal cycles in the course of welding, to temperatures in the range of 500 to 900°C in which σ-phase formation could occur. But in the present surfacing conditions—since dwell time at these temperatures did not reach the required minimum for the beginning of the transformation of δ-ferrite into σ-phase approximately 30 to 40 seconds (Ref. 15)—no σ-phase was present.

Analysis of Ferrite Content

It is an accepted practice to specify a minimum content of δ-ferrite in the austenitic clad or weld metal, to reduce solidification cracking tendency. Again depending upon the service conditions and considering the possibility of sigma phase formation, a maximum content of δ-ferrite is prescribed in different codes and specifications. The minimum recommended ferrite contents for 316L and 309L stainless steels are respectively 2% and 5% (Refs. 16, 17).

The ferrite content was estimated using Schaeffler, Delong and WRC-92 Constitution Diagrams and Seferian equation based on Schaeffler Equivalents depicted in Table 5 and were tabulated as shown in Table 3 to compare the estimated and the predicted values of ferrite content. Also, the values of WRC Ferrite Number corresponding to the measured ferrite content were found by linear interpolation from the Delong diagram (Ref. 18), and are given in Table 3. From Table 3, it is evident that the δ-ferrite content evaluated by various methods did not have same value but all values are very close to one another. It is to be noted that the prediction accuracy of the Schaeffler and Delong diagrams was +4% and ±2% respectively (Refs. 1, 10) and the accuracy of WRC-1992 diagram was claimed to be higher than that of Delong diagram (Ref. 3). Also, from Table 3, it is apparent that the ferrite content increased with increase in the $Cr_{equ.}/Ni_{equ.}$ ratio which was in agreement with the earlier reported results (Ref. 19). This may be due to the fact that the mode of solidification changes from the austenitic mode to ferritic mode when the ratio of $Cr_{equ.}/Ni_{equ.}$ is above 1.48 and hence room temperature ferrite content increases.

Microstructural Analysis

Using the color etching method with etchant 2(a), the interior of the cell becomes blue colored, while the borders of the cell appear brown or yellowish. Depending on the orientation of growth of the cells and direction of sectioning, the cell colonies appear as stripes or dots as shown in Fig. 11 (Ref. 20). A primary grain boundary lies where two cell colonies meet. From the position of the ferrite, in the interior or borders of the cells, as described below, it will be rec-

Fig. 12—Optical micrograph showing solidification structure of 309L buffer layer at 100X (A and AF modes of solidification) (J4).

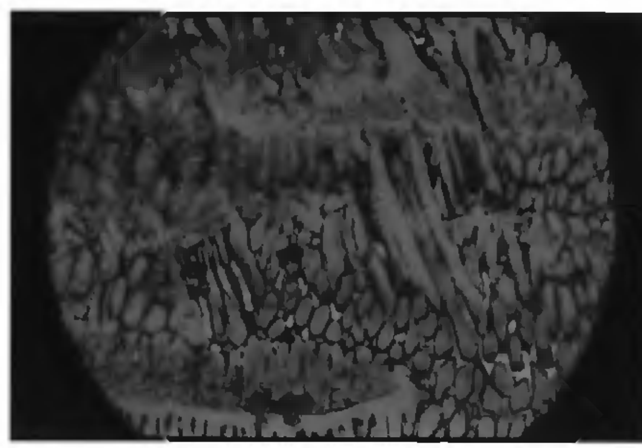

Fig. 13—Microstructure near fusion boundary showing mixed modes of solidification (austenitic + eutectic) (J1, 400X).

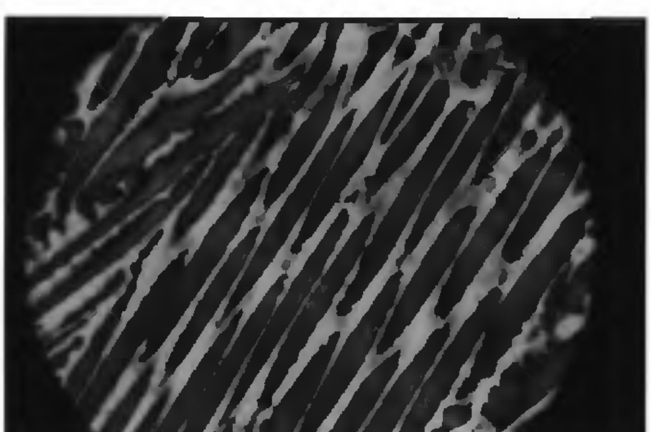

Fig. 14—Microstructure of 316L SS cladding showing primary austenitic solidification mode (J1, 400X).

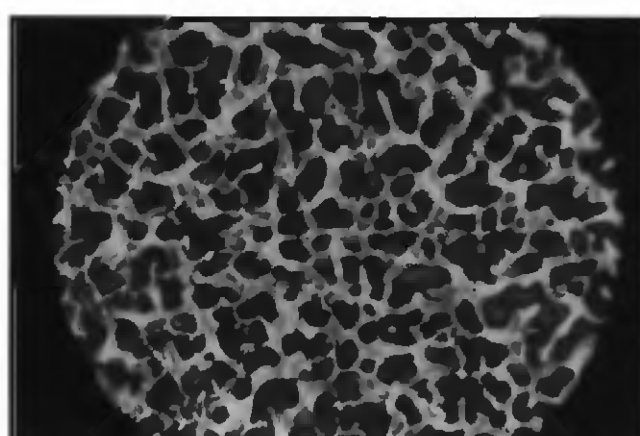

Fig. 15—Microstructure of 316L SS cladding showing eutectic solidification mode (J7, 400X).

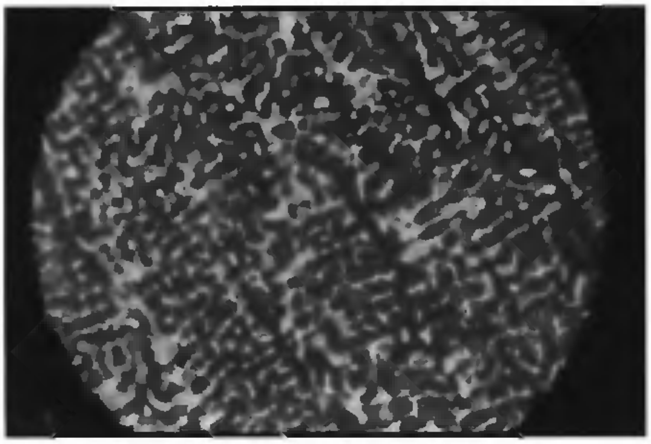

Fig. 16—Microstructure of 316L SS cladding showing eutectic solidification mode (J7, 400X).

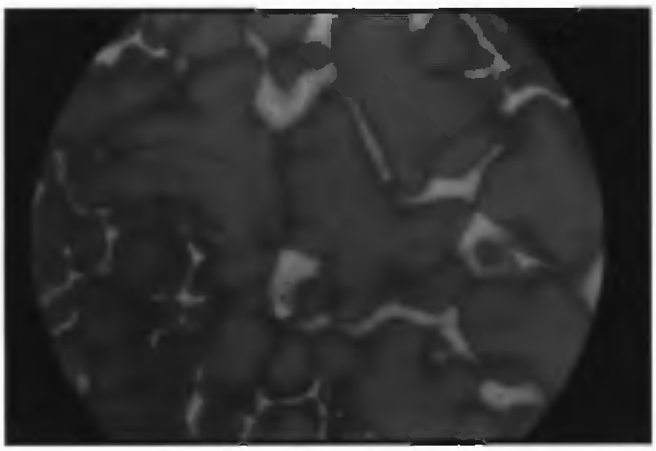

Fig. 17—Microstructure of 316L SS cladding showing eutectic solidification mode (J4, 1000X).

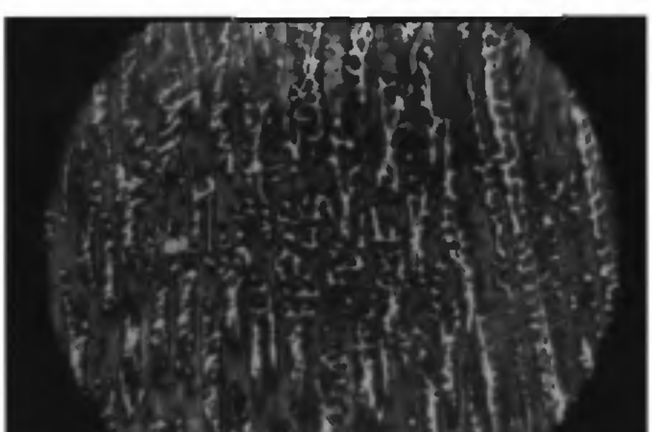

Fig. 18—Optical micrograph showing primary solidification mode with mixed ferrite morphology (vermicular and lathy) in 309L SS cladding (J7, 400X).

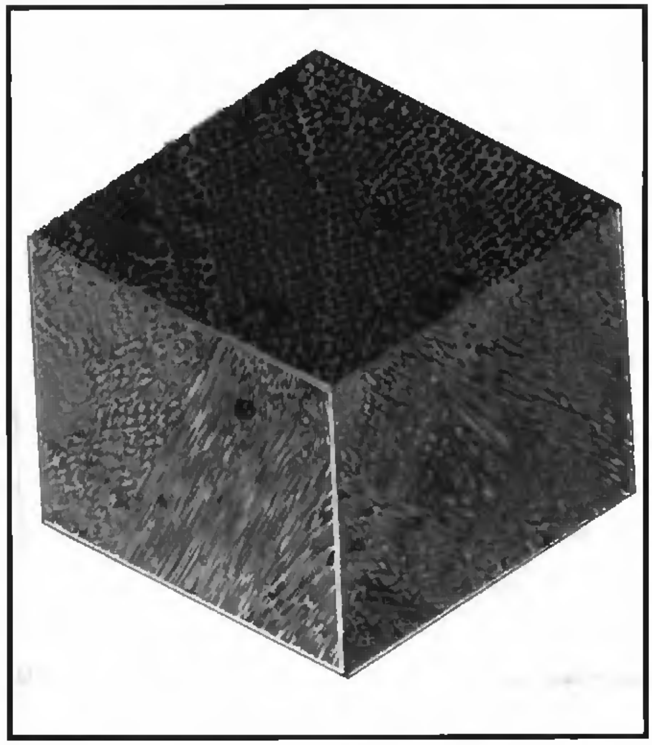

Fig. 19—Microstructure of single layer 316L SS cladding viewed content based on three mutually perpendicular directions (J1, 100X).

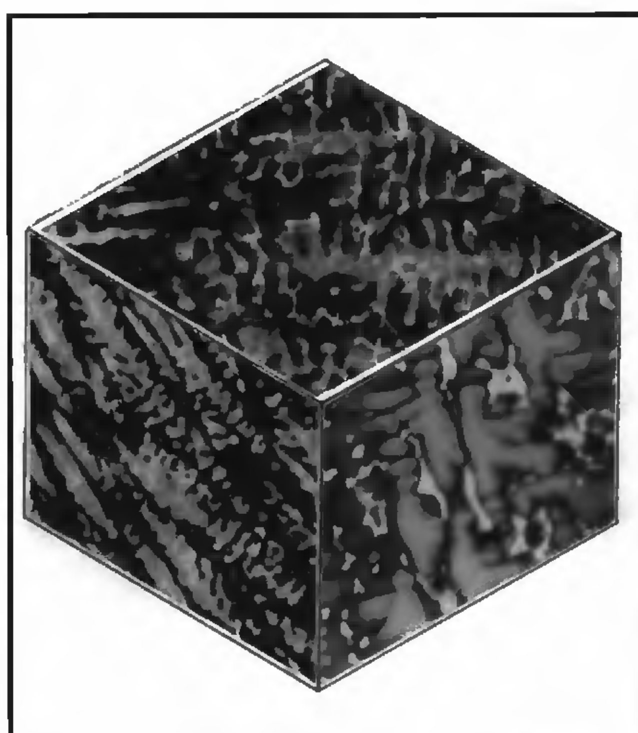

Fig. 20—Microstructure of single layer 316L SS cladding viewed content based on three mutually perpendicular directions (J4, 400X).

Fig. 21—Microstructures of 316L SS cladding showing the effect of multipass welding (M21, 100X).

ognized that the weldment solidified as ferrite or austenite respectively.

Optical color metallography revealed evidence of three types of solidification modes, which occurred in different samples as depicted in Figs. 12–21:

1) primary austenitic,

2) primary ferritic, and

3) eutectic (austenitic-ferritic, ferritic-austenitic).

These photographs were enlarged to four times their original magnification while printing; magnifications indicated in figures correspond to original magnification at which photomicrographs were obtained. These photomicrographs show characteristic primary solidification structures as they appear in different zones of a weld bead of austenitic stainless steel cladding with normal cooling in air. The solidification substructure was found to be mainly cellular or cellular-dendritic. However, narrow zones of planar growth were found along the fusion line. No equiaxed grains were found in weld metal.

Primary Austenitic Solidification

The photomicrograph shown in Fig. 12 depicts the characteristic solidification structures as they appear in the fusion zone of the buttering layer of 309L stainless steel. The photomicrograph was taken at 100X magnification along a section which was parallel to welding direction. The weld solidified initially with cellular structure and then gradually changed to cellular-dendritic structure depending upon the cooling rate. This was of austenitic plus austenitic-ferritic mode of solidification. The former occurred near the fusion boundary, followed by the latter. Near the fusion line, the primary structure was fully austenitic which had solidified to primary γ-crystals, and beyond this the austenite was the primary solidifying or leading phase and delta ferrite, if any, solidified from the rest of the melt at cellular or cellular dendritic substructure boundaries. This resembles the type A structure of solidification modes of austenitic stainless steel classified by Takalo *et al.* (Ref. 21). In this photomicrograph, the secondary grain boundaries formed by recrystallization after solidification can be identified by dark blue colored coarse grains near the fusion boundary.

Figure 13 is a typical photomicrograph taken along a section transverse to welding direction depicting mixed modes of solidification of 316L stainless steel cladding (J1). The magnification used was 400X. The apparent modes of solidification are fully austenitic and eutectic (austenitic-ferritic plus ferritic-austenitic). In fully austenitic mode (lower right corner), weldment solidified with initial cellular austenitic structure colored brown to bluish and the final solidification regions are white to yellowish. The blue colored cellular crystals show a slightly wavy surface, indicating the beginning of dendritic crystal formation. Ferrite is not present in the structure. Such a type of austenitic solidification mode is more apparently visible from Fig. 14. This photomicrograph of transverse section at 400X magnification was taken from the test samples J1.

Eutectic Solidification

In eutectic solidification represented at the top and left side center of the photomicrograph shown in Fig. 13, there are two types of solidification modes depending upon the alloy compositions lying on the ferritic side or on the austenitic side of the eutectic triangle as shown in Fig. 1A. In the first case, solidification begins with the formation of ferritic cells with austenite being formed in the border regions of the cells. Ferrite transforms in the solid state partially into austenite. Therefore, in certain cases, at room temperature, two different kinds of austenite are in the microstructure. In Figs. 13 and 15–17, the first ferrite to be formed lies in the interior of the blue colored austenite cell. The borders of the cells now are partly bluish, partly yellowish-white colored. In this case, the brownish borders correspond to austenite which is Ni-enriched compared with the austenite in the interior, both originating from the ferrite transformation. The still more Ni-enriched eutectic austenite, formed directly out of melt, appears yellowish-white and lies also at the grain boundaries.

In the second case of austenitic-ferritic mode, solidification begins with the formation of γ-crystals, the eutectic ferrite is therefore expected at the borders of the cells. This microstructure corresponds to the alloy lying on the Nickel rich side of the eutectic triangle (Fig. 1A) consisting of ferrite in the light borders of the cell, while the blue colored interior is free from ferrite as represented in Figs.13, 15, and 17. Also, grain boundaries of coarse grains formed by recrystallization after solidification can be seen near the left corner of Fig. 13 which overlap many primary precipitated small crystal cells (Ref. 12).

Primary Ferritic Solidification

The photomicrograph shown in Fig. 18 represents the characteristic primary solidification structure as it appears in the austenitic stainless steel (309L) weld metal of the buttering layer in a multilayer cladding (J7). The photograph was taken at 400X magnification along a section which was parallel to the welding direction. The weld solidified with two morphologies characterized by vermicular ferrite (right side of photograph) as well as lathy ferrite (left side) both located at the cell axes. This was of ferritic-austenitic (FA) solidification mode often termed as primary ferrite solidification: the leading phase was the δ-ferrite and austenite solidified from the melt and also through a solid-state δ-γ transformation occurring at high temperature. The average ferrite content of this cladding was 6.65%, as measured by using ferritescope. The blue areas of the structure represent the already solidified cellular crystals consisting of primary delta ferrite. In between is the residual melt which appears as a brownish tinted structural constituent. The blue color cellular crystals show a slightly wavy surface, indicating the beginning of dendritic crystal formation. A bright structural constituent is also visible in the primary precipitated delta ferrite crystals. This represents the residual delta ferrite which remains after δ-γ transformation. It was also observed that ferrite morphology changed from discontinuous vermicular type to continuous vermicular and lathy type as the ferrite content increased. These observations are in good agreement with results from the published literature (Refs. 16, 22) on the influence of ferrite content on its morphology in some austenitic weld metals.

Figures 19 and 20 depict the microstructures observed at sections mutually perpendicular to each other as described in Fig. 4 respectively at 100X and 400X magnifications of specimens J1 and J4. Figure 19 shows primary austenitic mode of solidification in three directions. Figure 20 indicates both primary ferritic and eutectic modes of solidification.

Effect of Multipass Welding on Microstructure

Figure 21 depicts the effect of multipass welding on the cellular dendritic structure of weld metal. Grain size decreased at the reheated portion of the weld metal. Photomicrograph was taken across sections transverse to welding direction at 100X magnification and the specimens were etched with the etchant 2(b) described in section 2.6.

Prediction of Modes of Solidification

The microstructure of a stainless steel weld is dependent on both the solidification mode and δ-γ transformation on cooling. Kujanpää, *et al.* (Ref. 23), has reported that when the ratio of Cr_{equ}/Ni_{equ} based on Schaeffler Equivalent is ≤ 1.48, austenitic or austenitic-ferritic solidification occurs, and if the ratio is between 1.48 and 1.95, ferritic solidification takes place. But Suutala (Ref. 24) has shown that the transition from primary austenitic to primary ferritic solidification in stainless steel welds occurs at a (Cr/Ni) equivalent ratio based on Hammer and Svensson Equivalents of 1.55. From the calculated potential factors of claddings given in Table 5, the values of Cr_{equ}/Ni_{equ} based on Schaeffler and Hammer and Svensson Equivalents were calculated and the modes of solidification of claddings were predicted based on these ratios of equivalents and also from WRC-1992 Constitutional Diagram. These predicted modes of solidification and the observed modes of solidification were tabulated as shown in Table 6 for ease of comparison. It is evident from the table that the predicted modes of solidification are well in agreement with the observed modes of solidification in most of the claddings.

EPMA and SEM Studies

Concentrations of the different elements across the transition zone and along the dendrites of delta iron—obtained by line scanning method in graphical form with the help of a graphics plotter provided along with the Microprobe Analyzer—are shown in Figs. 22–24.

It is well apparent from Fig. 22 that the intensities of Cr and Ni steadily increase from the base metal side to weld metal, but the intensity of Fe gradually decreases. Also, the intensities of Mo, Mn and Si increase very slightly along the transition zone. It is also evident from the figure that very small zones exist along the fusion line which are of intermediate composition between the carbon steel base metal and the bulk weld metal composition. These intermediate composition regions are referred to as intermediate mixed zones (IMZ) (Ref. 25) or transition zones.

Figure 23 is a typical concentration profile in which not only whole transition zone is covered but also some portions of both weld metal and base metal for obtaining concentration profiles. Figure 24 depicts the photomicrograph taken with the help of SEM at 800X magnification showing the line of trace along which the concentration profiles of Fig. 23 were taken. The intensities of Cr and Ni steadily increased from base metal side to weld metal up to a point which is 21 microns from the origin of the graph as shown; at the same time the intensity of Fe decreased gradually up to the same point. Beyond this point, the intensities of Cr and Ni fluctuated continuously in a systematic manner in such a way that whenever the intensity of Cr increased the intensity of Ni decreased and vice versa. This is obviously due to the segre-

Table 6—Comparison of Predicted and Actual Primary Solidification Modes in Stainless Steel Claddings

			Predicted Mode				
Sl. No.	Sample Code	SR	SMS	HR	SMH	SMW	Observed Mode
1	J1	1.38	A/AF	1.23	A/AF	AF	A/AF
2	J2	1.45	A/AF	1.23	A/AF	AF	AF/FA
3	J3	1.49	FA	1.33	A/AF	FA	FA
4	J4	1.68	FA	1.42	AF	AF	AF
5	J7	1.45	A/AF	1.29	A/AF	AF	AF/FA
6	J8	1.53	FA	1.35	A/AF	AF	AF/FA

SR = Ratio of $Cr_{equ.}/Ni_{equ.}$ based on Schaeffler Equivalents
HR = Ratio of $Cr_{equ.}/Ni_{equ.}$ based on Hammer and Svensson Equivalents
SMS = Predicted solidification mode based on SR
SMH = Predicted solidification mode based on HR
SMW = Predicted solidification mode based on WRC-1992 constitutional diagram
A = Austenitic mode of solidification
AF = Austenitic-ferrite mode of solidification
FA = Ferritic-austenitic mode of solidification